Short-Term Landslide Displacement Detection Based on GNSS Real-Time Kinematic Positioning

Nan Shen, Liang Chen, Lei Wang, *Member, IEEE*, Hao Hu, Xiangchen Lu, Chuang Qian, Jingbin Liu, Shuanggen Jin, *Member, IEEE*, and Ruizhi Chen

Abstract—Global navigation satellite system (GNSS) is one of the most effective means for landslide monitoring. At present, most studies on GNSS-based landslide monitoring focus on the long-term landslide analysis, while short-term landslide displacement is not clear. The purpose of this article is to explore a short-term displacement detection method based on GNSS kinematic positioning for landslide monitoring. The significance and feasibility of short-term landslide monitoring are presented, and a short-term displacement detection method based on GNSS kinematic positioning time series segmentation is proposed. The coordinate time series is reconstructed by the Daubechies wavelet to extract the abrupt components. The detection window is formed by the current epoch coordinates and the previous epochs' coordinates and segmented according to the segmentation index. The segmentation point obtained by segmenting the detection window is regarded as a possible change point (PCP), and a test is conducted to determine whether the segmentation point is a change point (CP). Simulation and field experiments were carried out to verify the proposed method. The results show the feasibility and effectiveness of the method for short-term landslide change detection. The influence of the detection window size and segmentation index on the proposed method is discussed, and suggestions for the selection of detection window size as well as segmentation index are given.

Index Terms—Global navigation satellite system (GNSS), kinematic positioning, landslide, short-term displacement detection, segmentation.

I. INTRODUCTION

LANDSLIDE is a natural phenomenon in which the soil or rock mass on the slope slides downward in a whole or scattered manner under the influence of rainfall, earthquake, and other factors [1]. It is one of the most damaging and deadly natural hazards [2]. In the last two decades, there has been a surge of interest in investigating the global navigation satellite system (GNSS) for landslide monitoring. Compared with the traditional landslide monitoring technology, GNSS observation has the following technical advantages:

independent of the weather, no requirement for visibility between monitoring points, high accuracy, and diverse time scales [3]. Besides, with the continuous development of GNSS technology, the cost of the receiver is decreasing, and the positioning accuracy has been significantly improved [4].

Previous landslide surface displacement monitoring was a simple but effective method for landslide monitoring and analysis [5]. There are a large number of studies that presented the applications of GNSS for landslide monitoring. Gili *et al.* [6] first examined the feasibility of the global positioning system (GPS) applied to landslide monitoring, in which more than 26 months of GPS observation data were used to calculate the displacement. Compared with the measurement results of electronic distance meters, inclinometer, and wire extensometer, the GPS measurement has the horizontal accuracy of 12–16 mm and the vertical accuracy of 18–24 mm. Abidin *et al.* [7] conducted a repeated GPS survey to detect land displacements in the landslide-prone area and obtained the landslide displacement by the coordinate difference between two consecutive GPS measurements, which showed that the GPS was a reliable method for studying and monitoring landslide displacement. To determine the experimental accuracy of GPS measurements for continuous landslide monitoring, Su *et al.* [8] installed three GPS receivers to measure ground displacement in the landslide area. By comparing with surface extensometers data on-site, the results showed that GPS could be used for long-term monitoring of high-mountain landslides. To evaluate the feasibility of rapid static and relative real-time kinematic (RTK) for landslide monitoring, Rawat *et al.* [9] conducted a study in the case of Bakthang landslide, Gangtok, East Sikkim, India. The result indicated that these techniques were very reliable for landslide monitoring. Similarly, Wang [10] conducted a comparative study on a single station and network solutions for long-term landslide monitoring [11], which showed that the network solution was more favorable to eliminate gross errors and improve the accuracy and robustness of landslide monitoring. Lytvyn *et al.* [12] proposed using the single-frequency precise point position (PPP) for landslide monitoring and developed a landslide monitoring system based on single-frequency PPP. To reduce the cost of landslide monitoring, Xiao and He [13] proposed GPS multiantenna switching technology and developed a multiantenna monitoring system. The experimental results showed that for long-term landslide monitoring, the accuracy level of multiantenna switching was comparable to that of the single antenna single receiver. Overall, the studies described above are mainly concerned with the feasibility of GPS for long-term landslide monitoring.

There are few high-quality studies dedicated to short-term landslide monitoring. Li and Kuhlmann [14] proposed a multiple Kalman filter model to capture the abrupt, in which different filters represent different deformation types. However, the coordinate time series were processed epoch by epoch, which was easily affected by measurement errors. To evaluate whether the mass-market GNSS receiver is suitable for short-term landslide monitoring, Cina and Piras [15] used a special metal slide to simulate the landslide and the vertical and horizontal displacement of the antenna that could be fine-tuned by micrometers. A control experiment of single-frequency GNSS receiver accuracy evaluation was carried out by using this device. The results showed that under certain conditions, the accuracy of single-frequency GNSS can reach millimeter, which is suitable for landslide displacement monitoring. However, in their study, the mechanism of change detection was not described in detail. Bellone *et al.* [16] conducted a similar study using the same device to evaluate the single-frequency receiver Ublox and the geodetic receiver. The data collected from these receivers were processed in the network RTK positioning mode, and then, the Chow test was performed on the positioning results. The results showed that the Chow test was an effective displacement detection tool. However, only ultrashort baseline experiments were carried out, and the selection strategy of window size for the statistical test was not given. Besides, Dabove and Manzino [17] proposed a cluster-based method for dynamic deformation analysis, but this method did not perform well on real data. These studies mentioned above were of some significance to short-term landslide monitoring, but there are some limitations.

Studies over the past two decades have provided important information on GNSS-based landslide monitoring, but most of which are only suitable for offline application. Up to now, less research has been carried out on short-term displacement detection. Although the displacement can be directly obtained by the difference between GNSS coordinates, it is still a challenge to detect the change and extract the displacement effectively in a short time due to the influence of measurement error. At present, the displacement detection process of most existed methods is carried out epoch by epoch, which is easily affected by the gross error and observation noise [18].

This article proposes a new methodology for displacement identification and extraction. The primary aim of this study is to find a straightforward and feasible displacement detection method based on GNSS kinematic positioning, which can be used for short-term landslide monitoring. The approach taken in this study is a mixed methodology based on the GNSS kinematic positioning and time series segmentation. The time series obtained from GNSS kinematic positioning is used as the basic processing unit. Before displacement detection, the Daubechies wavelet is used to reconstruct the signal and extract the abrupt component. Then, the detection window is formed and segmented according to the segmentation index to find the possible change point (PCP). Finally, a test is performed to determine whether the segmentation point is a change point (CP). The experimental work presented here is one of the first investigations to explore short-term displacement identification and extraction from the GNSS
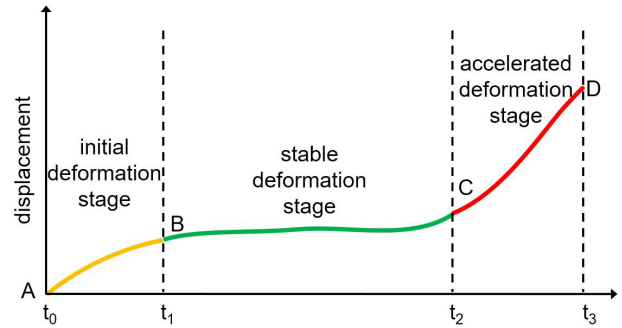

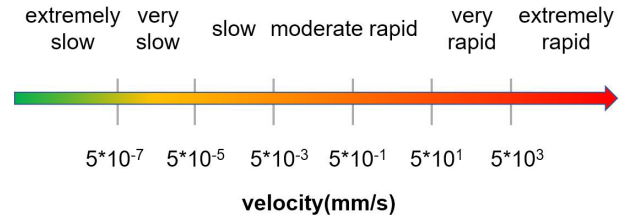Fig. 1. Ideal diagram of slope body displacement [19].

Fig. 2. Landslide grade according to velocity.

real-time kinematic positioning by time series segmentation. The remaining part is as follows. Section II shows the methodology used for this study, Section III presents the experimental results, the discussion is given in Section IV, and finally, the conclusion is given in the last section.

II. METHODOLOGY

In this section, the concept of landslide short-term monitoring is presented first. Then, displacement detection based on time series segmentation is proposed, and GNSS kinematic positioning is introduced. Finally, the workflow of displacement detection by time series segmentation of the GPS real-time kinematic positioning is given.

A. Landslide Short-Term Monitoring

According to the monitoring data of a large number of landslide examples, the spatial change characteristics of the slope can be summarized, as shown in Fig. 1. The evolution of a slope into a landslide generally undergoes three deformation stages [19]: the initial deformation stage, the stable deformation stage, and the accelerated deformation stage. During the initial deformation phase, deformation begins to form, and as time goes by, the deformation slows down and enters the stable phase. In the stable deformation stage, the deformation is slow, and long-term monitoring is generally carried out at this stage. In the accelerated deformation stage, the deformation rate increases continuously until the landslide occurs. Studies show that the accelerated deformation stage of the slope is the basis and prerequisite for the occurrence of landslides [19], [20]. Therefore, the accelerated deformation stage of the slope is of great significance to landslide prediction [19]. Besides, the landslide can be divided into six grades according to the landslide velocity [21], as shown in Fig. 2. We define short-term landslide monitoring as slope displacement acceleration deformation stage monitoring, or slow, moderate, and rapid landslide monitoring. The purpose of short-term
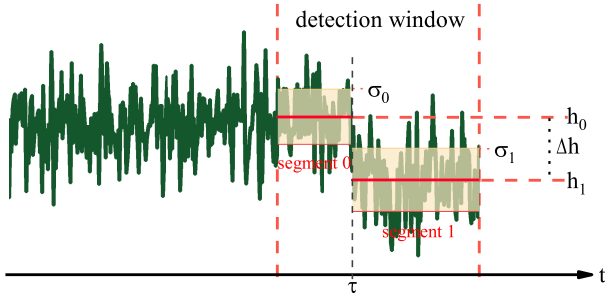
Fig. 3.   Schematic of displacement detection based on time series segmentation.

monitoring is to provide early warning of landslides, and GNSS kinematic positioning mode is recommended [22]. According to the monitoring data of landslide cases [20], [23], the overall trend of the deformation time curve conforms to the above three-stage evolution law, but it is not as smooth as in Fig. 1 [19], [20], and the local is often stepped [19]. Therefore, in the following, displacement detection is aimed at the abrupt displacement.

B. Displacement Detection Based on Time Series Segmentation

A time series window is expressed as $x_1, x_2, \ldots, x_n$, where n is the size of the window. For a classical time series segmentation problem, it is assumed that there are m change points in the time series, and the corresponding sequence number is $\tau = [\tau_1, \tau_2, \ldots \tau_m]$. The entire time series is divided into $m + 1$ segments by these m change points. The statistical mean value of each segment is expressed as follows:

$$\bar{x}(k) = \frac{1}{\tau_{k+1} - \tau_k} \sum_{j=\tau_k}^{\tau_{k+1}-1} x_j \tag{1}$$

where τ_0 and τ_{m+1} are defined as $\tau_0 = 1$ and $\tau_{m+1} = n + 1$, respectively, and $k = (0, 1, \ldots, m)$ denotes the kth segment.

For the short-term displacement detection of landslides using GNSS, more attention is paid to the time and degree of change, rather than segmenting the entire time series. Besides, multichange point detection is generally computationally intensive and not suitable for online implementation. Therefore, the detection window as shown in Fig. 3 is defined for short-term displacement detection. As shown in Fig. 3, the mean and variance of the two segments divided by τ are expressed as h_0 and h_1 and σ_0^2 and σ_1^2, respectively. Then, the displacement before and after the change point can be estimated as follows:

$$\Delta h = h_0 - h_1. \tag{2}$$

After defining such a detection window, the first task is to find the most likely segmentation point or the PCP according to the detection index. Therefore, various detection indices are introduced in the following.

C. Detection Window Segmentation Indices

There are many different indices for window segmentation, the most commonly used ones are introduced here. Window segmentation based on these indicators is the state-of-the-art segmentation methods in time series segmentation. However, the segmentation points obtained by these segmentation methods are called PCP here. These PCPs are not necessarily CP due to local disturbance. The final CP will be determined based on these PCP statistics. In the experimental section, the direct PCP output of these segmentation methods will be given as a comparison.

1) Variance Test (VT): For time series segmentation, the objective function is constructed based on the statistic of each section, and the most common statistical value is the variance [24], [25]

$$J(\tau) = \sum_{k=0}^{m} \sum_{i=\tau_k}^{\tau_{k+1}-1} (x_i - \bar{x}(k))^2 \tag{3}$$

where $J(\tau)$ represents the objective function. The meaning of other symbols is consistent with that in Section II-B. For the window segmentation problem described above, the objective function is simplified as follows:

$$J(\tau) = \sigma_0^2 + \sigma_1^2 = \sum_{i=1}^{\tau-1} \left(x_i - \frac{1}{\tau-1} \sum_{j=1}^{\tau-1} x_j \right)^2$$
$$+ \sum_{i=\tau}^{n} \left(x_i - \frac{1}{n-\tau+1} \sum_{j=\tau}^{n} x_j \right)^2 \tag{4}$$

in which τ is the PCP that needs to be estimated in each detection window. Then, the PCP detection problem is transformed into

$$\hat{\tau} = \arg \min_{\tau} J(\tau), \quad 2 \leq \tau \leq n \tag{5}$$

where $\hat{\tau}$ represents the optimal estimate. For any detection window, a value τ can always be found to minimize the above formula, that is, the segmentation point is not necessarily a CP. How to determine CP based on PCP statistics will be introduced later.

2) Standard Normal Homogeneity Test (SNHT): SNHT is one of the widely used anomaly detection methods in hydrometeorology, which is used to study the inhomogeneities in the mean value of the observations [26]. The test statistic is

$$\hat{\tau} = \arg \max_{\tau} [(\tau-1)\bar{x}(0)^2 + (n-\tau+1)\bar{x}(1)^2], \quad 2 \leq \tau \leq n \tag{6}$$

where $\bar{x}(0)$, $\bar{x}(1)$ can be obtained according to (1). Similar to the index VT introduced above, this formula can only determine PCP, and further decision on CP is needed.

3) Pettit's Test (PETT): Pettit's test is a nonparametric approach to the change-point problem, and the test statistic is [27]

$$U_{\tau,n} = U_{\tau-1,n} + \sum_{j=\tau+1}^{n} \text{sgn}(x_\tau - x_j), \quad 2 \leq \tau \leq n \tag{7}$$

where

$$
\operatorname{sgn}(x_i - x_j) \triangleq
\begin{cases}
1, & x_i - x_j > 0 \\
0, & x_i - x_j = 0 \\
-1, & x_i - x_j < 0.
\end{cases}
$$

Under the null hypothesis, for each τ, the distribution of $U_{\tau,n}$ is symmetric about zero, that is, $E(U_{\tau,n}) = 0$. The segmentation point corresponding to the statistic with the largest absolute value is considered to be the most likely change point

$$
K_{\hat{\tau},n} = \max \left| U_{\tau,n} \right|, \quad \tau = 1, 2, \ldots, n. \tag{8}
$$

The significant probability of $K_{\hat{\tau},n}$ is approximately calculated as

$$
p \simeq 2 \exp\left(\frac{-6 K_{\hat{\tau},n}^2}{n^3 + n^2} \right). \tag{9}
$$

The probability of PCP as CP can be obtained according to the statistical value.

4) Z Test (ZT): The Z test is often used to detect the significance of the mean difference, and the test statistic is defined as follows:

$$
\begin{aligned}
Z_\tau &= \frac{h_1 - h_0}{\sqrt{\frac{\sigma_0^2}{\tau - 1} + \frac{\sigma_1^2}{n - \tau + 1}}} \\
&= \frac{\Delta \hat{h}}{\sqrt{\frac{\sigma_0^2}{\tau - 1} + \frac{\sigma_1^2}{n - \tau + 1}}}, \quad 2 \le \tau \le n. \tag{10}
\end{aligned}
$$

The test statistic is also called the z score. The segmentation point corresponding to the maximum absolute z score is considered to be the most likely change point

$$
\hat{\tau} = \arg \max_\tau |Z_t|, \quad 2 \le \tau \le n. \tag{11}
$$

The probability of PCP becoming CP can be obtained according to the statistical value, which is assumed to follow the standard normal distribution.

For a certain detection window, a PCP can always be found through the above tests. As for whether the epoch corresponding to the PCP is a CP, continuous tracking and statistics of the epoch are required, which will be introduced next.

D. PCP Statistics

The detection window formed by the current observation epoch and several previous epochs is segmented according to the indices described above, and the PCP of the current detection window is found. It is necessary to further determine whether the PCP is a CP. For the detection window of size n, the number of times an epoch participates in the window segmentation is n, which starts from the epoch entering the detection window to leaving the detection window completely. In the process of window segmentation, the more times the epoch is divided into PCP, the more likely it is to be a CP. The statistic count_i is defined as the number of times that the epoch i is divided into PCP. If the count_i of an epoch is greater

than a certain threshold, the epoch is regarded as a CP. The uncertainty of the epoch i identified as the change point is

$$
u\_cp_i = \frac{n - \text{count}_i}{n} \tag{12}
$$

where u_cp_i is defined as the percentage of PCP that cannot support the ith epoch as the change point; $n - \text{count}_i$ denotes the number of times that the epoch i is not divided into PCP for the detection window of size n. It can be seen from the definition that for a fixed detection window, the greater the statistical count, the smaller the uncertainty.

For an epoch with count_i PCPs, there are also count_i displacement estimates, which is expressed as follows:

$$
\Delta h_{ij} = h_{ij0} - h_{ij1}, \quad 1 \le j \le \text{count}_i \tag{13}
$$

where Δh_{ij} is the jth displacement estimate of the ith epoch; h_{ij0} and h_{ij1}, respectively, represent the mean value of the coordinates of the two parts of the window segmentation, as shown in Fig. 3. Since count_i PCPs correspond to count_i segmentation windows, it is impossible to evaluate the reliability of these displacement estimates using indices described above. Similar to the determination of CP, the more concentrated Δh_{ij} is, the closer it is to the true value. Based on this idea, the displacement is divided into equal intervals according to the displacement estimation range of PCPs

$$
bin_{ik} = \operatorname{div}\left(\min(\Delta h_{ij}), \max(\Delta h_{ij}), s \right), \quad 1 \le k \le s \tag{14}
$$

where the $\operatorname{div}(x_1, x_2, s)$ operator indicates generating s intervals, and the interval width is $((x_2 - x_1)/s)$. Then, based on the count the number of Δh_{ij} falling into each interval, the final displacement estimate is

$$
\widehat{\Delta h_i} = f\left(\arg \max_{bin_{ik}} (\text{count}(bin_{ik})) \right) \tag{15}
$$

where s is the number of intervals divided and $\text{count}(bin_{ik})$ denotes the number of Δh_{ij} falling into bin_{ik}. f is the mapping function from displacement interval to displacement. In this work, s is set to 100, and f is defined as the mean of the displacement interval. It can be seen from (2) and Fig. 3 that the uncertainty of the extracted displacement is determined by the uncertainty of the mean of the segments

$$
u\_disp_i = \sqrt{\sigma_0^2 + \sigma_1^2}. \tag{16}
$$

It is assumed that the variance of single-epoch observations is σ and independent of each other. Then, the variances of segment 0 with n_0 observations and segment 1 with n_1 observations are

$$
\sigma_0^2 = \frac{\sigma^2}{n_0} \tag{17}
$$

$$
\sigma_1^2 = \frac{\sigma^2}{n_1}. \tag{18}
$$

Then, the uncertainty of the extracted displacement is

$$
u\_disp_i = \sqrt{\frac{n_0 + n_1}{n_0 n_1}} \sigma. \tag{19}
$$

The following inequality exists between the number of observations of the two segments

$$(n_0 + n_1)^2 \geq 4n_0n_1. \tag{20}$$

According to (19) and (20), the lower limit of the extracted displacement uncertainty is obtained

$$u\_disp_i \geq \frac{2}{\sqrt{n}}\sigma. \tag{21}$$

From the above derivation, it can be seen that the uncertainty of the extracted displacement has no direct relationship with the displacement. The introduction of displacement detection based on time series segmentation is given above, and the source of time series is introduced next.

E. Relative Real-Time Kinematic (RTK)

RTK is widely used in structural health monitoring, landslide monitoring, and other fields due to its high positioning accuracy and real-time efficiency. The observation model, the state model, and the extended Kalman filtering process of RTK are introduced next.

1) Observation Model: The double-difference (DD) observation equation of relative positioning among base receiver, rover receiver, and satellites j and k is defined in (22), as shown at the bottom of the page [18].

In this observation equation, $\Delta\nabla$ denotes the DD operator, i denotes the frequency; b and r denote base station and rover station, respectively. $\Delta\nabla P_{i_{br}}^{jk}$ and $\Delta\nabla\Phi_{i_{br}}^{jk}$ denote pseudo-range and carrier-phase DD observations, respectively. $\Delta\nabla\rho_{br}^{jk}$ is the DD geometric distance between receivers and satellites. $\Delta\nabla M_{P_{i_{br}}}^{jk}$ and $\Delta\nabla M_{\Phi_{i_{br}}}^{jk}$ denote pseudo-range and carrier-phase multipath error, respectively. $\Delta\nabla\varepsilon_{P_{i_{br}}}^{jk}$ and $\Delta\nabla\varepsilon_{\Phi_{i_{br}}}^{jk}$ represent DD observation error of pseudo-range and carrier-phase, respectively. $\Delta\nabla I_{\Phi_{i_{br}}}^{jk}$ is the DD ionospheric delay between receivers and satellites, and the ionospheric error has the same absolute value but the opposite sign on pseudo-range and carrier-phase observations. $\Delta\nabla T_{br}^{jk}$ is the DD tropospheric delay between receivers and satellites. For the short baseline, the atmospheric error can be ignored, so the above DD observation equation is simplified as

$$\left.\begin{array}{l}\Delta\nabla P_{i_{br}}^{jk} = \Delta\nabla\rho_{br}^{jk} + \Delta\nabla M_{P_{i_{br}}}^{jk} + \Delta\nabla\varepsilon_{P_{i_{br}}}^{jk} \\ \Delta\nabla\Phi_{i_{br}}^{jk} = \Delta\nabla\rho_{br}^{jk} - \lambda_i\Delta\nabla N_{i_{br}}^{jk} + \Delta\nabla M_{\Phi_{i_{br}}}^{jk} + \Delta\nabla\varepsilon_{\Phi_{i_{br}}}^{jk}\end{array}\right\}. \tag{23}$$

By ignoring the influence of multipath, linearizing equation (23), we get

$$\mathbf{y} = \mathbf{Hx} + \varepsilon \tag{24}$$

where $\mathbf{y}$ is the observation minus the computed, $\mathbf{H}$ is the linearized design matrix [28], $\mathbf{x} \triangleq [\mathbf{r_r}, \Delta\nabla\mathbf{N}]^{\mathbf{T}}$ is the state vector, which contains the rover station coordinate $\mathbf{r}_r$ and the DD integer ambiguity $\Delta\nabla\mathbf{N}$; ε is the observation noise and its covariance matrix is expressed as $\mathbf{R}_\varepsilon$. After forming the

observation equation, the "float" solution of the parameter can be obtained by the standard least square method. To obtain high-precision positioning results, it is necessary to fix the integer ambiguity. The "float" solution and variance of integer ambiguity are expressed as $\Delta\nabla\tilde{\mathbf{N}}$ and $\mathbf{Q}_{\Delta\nabla\tilde{\mathbf{N}}}$, respectively. Then, the problem of ambiguity fixing can be described as (25) [29]

$$\Delta\nabla\hat{\mathbf{N}}$$
$$= \underset{\Delta\nabla\mathbf{N}\in\mathbf{Z}}{\arg\min}\left(\left(\Delta\nabla\mathbf{N} - \Delta\nabla\tilde{\mathbf{N}}\right)\mathbf{Q}_{\Delta\nabla\tilde{\mathbf{N}}}^{-1}\left(\Delta\nabla\mathbf{N} - \Delta\nabla\tilde{\mathbf{N}}\right)^T\right) \tag{25}$$

There are many methods referring to integer ambiguity resolution, among which LAMBDA (Least-squares Ambiguity Decorrelation Adjustment) [29] method is the most widely used one. The integer ambiguity is obtained by the integer least square method. Then, the test process is executed to determine whether to accept or reject the integer ambiguity [30], [31]. If the test is passed, the fixed integer ambiguity can be substituted into (24) to resolve the fixed solution; otherwise, the "float" solution will be maintained.

2) State Model: The state model is defined as follows [37]:

$$\mathbf{x}_k = \mathbf{Fx}_{k-1} + \mathbf{w} \tag{26}$$

where

$$\mathbf{F} \triangleq \begin{bmatrix} \mathbf{I}_{3\times3} & \mathbf{0} \\ \mathbf{0} & \mathbf{I}_{(2n-2)(2n-2)} \end{bmatrix}$$

is the transition matrix from epoch $k-1$ to epoch k, $\mathbf{I}$ denotes the identity matrix, and n represents the number of satellites observed simultaneously by the base station and the rover station. Only GPS L_1 and L_2 frequency observations are considered, so $2n-2$ DD ambiguities are formed. $\mathbf{w}$ is the process noise, and its covariance matrix is expressed as $\mathbf{G}_w$. For kinematic positioning, the coordinate covariance component is set to be large to capture dynamic features, while the ambiguity covariance component is set to $\mathbf{0}$ to ensure the stability of positioning.

3) Extended Kalman Filtering: Kalman filtering includes two processes: prediction update and measurement update [32]. The prediction process is as follows:

$$\hat{\mathbf{x}}_{k|k-1} = \mathbf{F}\hat{\mathbf{x}}_{k-1} \tag{27}$$
$$\mathbf{Q}_{k|k-1} = \mathbf{FQ}_{k-1}\mathbf{F}^T + \mathbf{G}_w(k) \tag{28}$$

where $\hat{\mathbf{x}}_{k|k-1}$ and $\mathbf{Q}_{k|k-1}$ represent the predicted value and the corresponding covariance, respectively. According to the definition of the state transition matrix above, it can be seen that the state value of the previous epoch remains unchanged. However, the coordinate covariance component becomes larger, while the ambiguity covariance component remains unchanged. The measurement update process is as follows:

$$\mathbf{v}_k = \mathbf{y}(k) - \mathbf{H}_k\hat{\mathbf{x}}_{k|k-1} \tag{29}$$
$$\mathbf{S}_k = \mathbf{H}_k\mathbf{Q}_{k|k-1}\mathbf{H}_k^T + \mathbf{R}_\varepsilon(k) \tag{30}$$
$$\mathbf{K} = \mathbf{Q}_{k|k-1}\mathbf{H}_k^T\mathbf{S}_k^{-1} \tag{31}$$

$$\left.\begin{array}{l}\Delta\nabla P_{i_{br}}^{jk} = \Delta\nabla\rho_{br}^{jk} - \Delta\nabla I_{\Phi_{i_{br}}}^{jk} + \Delta\nabla T_{br}^{jk} + \Delta\nabla M_{P_{i_{br}}}^{jk} + \Delta\nabla\varepsilon_{P_{i_{br}}}^{jk} \\ \Delta\nabla\Phi_{i_{br}}^{jk} = \Delta\nabla\rho_{br}^{jk} + \Delta\nabla I_{\Phi_{i_{br}}}^{jk} + \Delta\nabla T_{br}^{jk} - \lambda_i\Delta\nabla N_{i_{br}}^{jk} + \Delta\nabla M_{\Phi_{i_{br}}}^{jk} + \Delta\nabla\varepsilon_{\Phi_{i_{br}}}^{jk}\end{array}\right\} \tag{22}$$

where $\mathbf{v}_k$ denotes the innovation vector, $\mathbf{S}_k$ is the covariance matrix of the innovation vector, $\mathbf{H_k}$ is the design matrix at epoch k, and $\mathbf{K}$ is the state estimation gain matrix. The final state is estimated as follows:

$$\hat{\mathbf{x}}_k = \hat{\mathbf{x}}_{k|k-1} + \mathbf{K}\mathbf{v}_k \tag{32}$$

$$\mathbf{Q}_k = \mathbf{Q}_{k|k-1} - \mathbf{K}\mathbf{S}_k\mathbf{K}^T \tag{33}$$

where $\hat{\mathbf{x}}_k$ is the final estimate, $\mathbf{Q}_k$ is the corresponding covariance matrix, and $\hat{\mathbf{x}}_k$ is the only input of the proposed method.

Due to the complex spatiotemporal characteristics of observation errors, there are unmodeled error components in time series [33]. To weaken the influence of these factors, the wavelet analysis tool is introduced as follows.

F. Wavelet Analysis

A wavelet analysis has been developed for decades and is widely used in signal denoising, anomaly detection, data compression, and other fields [34]. Compared with the Fourier transform, wavelet analysis is a more effective time–frequency analysis tool. Wavelet analysis refines the signal step by step through stretching and translation operations and finally achieves time subdivision at high frequency and frequency subdivision at low frequency. It can automatically adapt to the requirements of time–frequency signal analysis, to focus on any details of the signal [35].

1) Wavelet Transform: The definition of continuous wavelet transform is as follows [35]:

$$\text{CWT}(a, b) = \frac{1}{\sqrt{a}} \int_{-\infty}^{\infty} x(t)\psi^*\left(\frac{t-b}{a}\right) dt \tag{34}$$

where a and b are scaling and translation factors, respectively. $x(t)$ is the time series to be analyzed. $\psi(\cdot)$ is the mother wavelet function, and $\psi^*(\cdot)$ is the conjugate of $\psi(\cdot)$. By adjusting the scaling factor a and translation factor b, the wavelet with different time–frequency width can be obtained to match any position of the original signal, to achieve the purpose of time–frequency localization analysis of the signal. The scaling factor and translation factor of continuous wavelet transform are real numbers, which is very inconvenient in engineering applications. Discrete wavelet transform (DWT) is often used in the numerical calculation of practical problems and is defined as follows [35]:

$$\text{DWT}(m, n) = \frac{1}{\sqrt{a_0^m}} \int_{-\infty}^{\infty} x(t)\psi^*\left(\frac{t}{a_0^m} - nb_0\right) dt \tag{35}$$

where the integers m and n are the scaling factor and the translation factor, respectively. a_0 is a specified fixed scaling step parameter, which is greater than 1, and b_0 is the location parameter, which must be greater than zero.

2) Wavelet Function: One of the most important problems in the application of wavelet analysis in engineering is the choice of mother wavelet because different mother wavelets will produce different results for the same problem. In this article, the purpose of the wavelet transform is to extract the abrupt component in the signal. Many different wavelet functions that fulfill this requirement can be used in practice. The work presented in this article utilizes the Daubechies wavelet function, which is constructed by Inrid Daubechies, a famous wavelet analysis scholar in the world. The wavelet basis in the Daubechies family is denoted as dbN, where N is the sequence, satisfying $N = 1,\ 2..10$. The regularization coefficient of the $db1$ wavelet has the greatest similarity with the Lipschitz index of the signal at the abrupt, which can most effectively characterize the abrupt [36]. Therefore, $db1$ is used as the basis function to decompose the original signal.

G. Workflow of Displacement Detection

In the previous paragraphs, landslide short-term monitoring is introduced, and the short-term displacement detection based on time series segmentation is proposed. The principle of relative real-time kinematic positioning and wavelet analysis are given. The flowchart of change detection by time series segmentation of the GPS real-time kinematic positioning is given in Fig. 4.

As shown in Fig. 4, to begin this process, the kinematic positioning is performed to obtain the coordinates time series to form the processing unit. Prior to displacement detection, the wavelet tool is used to denoise the processing unit. In Fig. 4, s denotes the original time series and a_i and d_i represent the approximation coefficients and detail coefficients, respectively. After obtaining the wavelet reconstructed time series, the whole process enters the displacement detection module. The so-called detection window is formed based on the coordinates of the current epoch and the previous several epochs. On getting the detection window, the window is segmented according to the indices, and a PCP can be obtained. Finally, test the PCP according to the PCP statistics to determine whether the PCP is a CP. Wavelet reconstruction is not a must because abrupt components may not be effectively extracted for small displacement, which will be seen in later experiments.

III. EXPERIMENTS AND RESULTS

To verify the feasibility of the proposed method, we carried out a series of experiments, including simulation experiments and field experiments. In the simulation experiment, data affected by noise and a trend item are simulated. In the field experiment, several displacement changes were triggered manually, and the relative real-time kinematic model is used to process the GNSS observations.

A. Simulation Experiments

In the simulation experiment, we only simulate the position measurement. GPS positioning results are affected by measurement noise, ionospheric delay, tropospheric delay, multipath effects, and other errors. Although combined observations or models are used to deal with these errors, there are still unmodeled trend term and observation noise in the final positioning results [33]. Therefore, the designed simulation data include observation noise, trend term, and specially designed abrupt displacement. The designed position measurement is affected by both the observation noise and a trend item. The trend item is defined as follows:
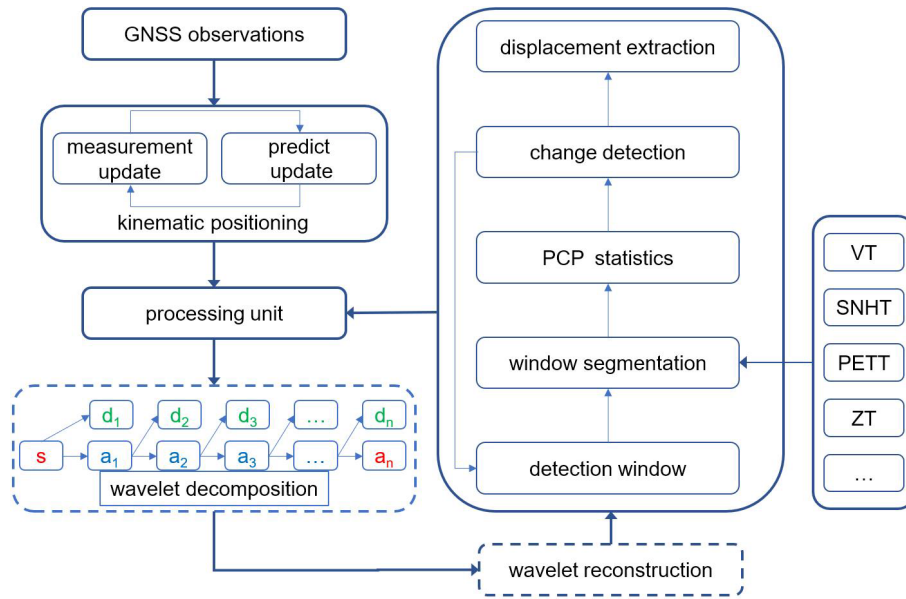
$$d_{\text{trend}} = 0.005t \tag{36}$$

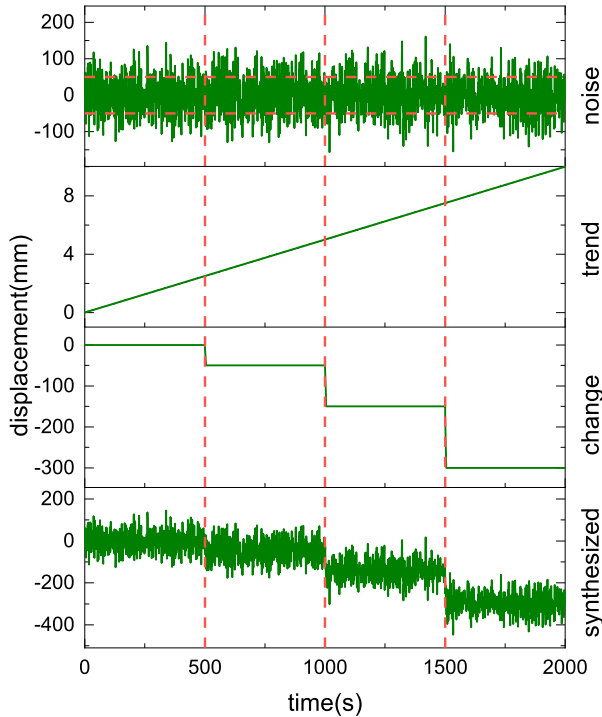Fig. 4. Workflow of displacement detection by time series segmentation of the GPS real-time kinematic positioning.
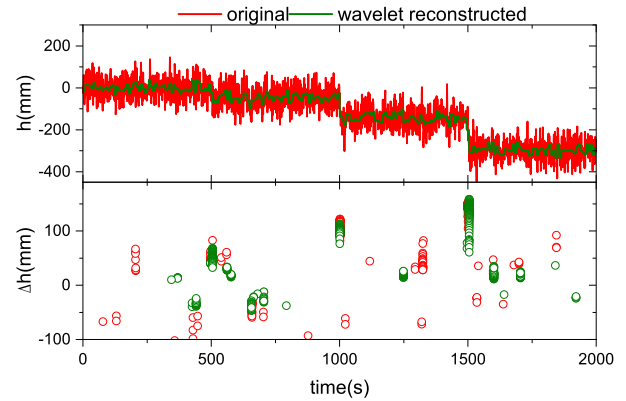

Fig. 5. Simulation data with multiple changes.

Fig. 6. Detection result of simulation data with VT as the index.

As shown in Fig. 5, the simulation data are synthesized by the Gaussian noise, the trend item, and displacement changes. The simulation data are processed by the method proposed above, and the displacement, PCPs are shown in Fig. 6.

As shown at the top of Fig. 6, after reconstructed by the designed wavelet, the time series shows more obvious abrupt characteristics. The bottom of Fig.6 shows the PCPs obtained by window segmentation, where the detection window size is 300. The influence of the detection window size on the detection results will be discussed later. From the above results, it can be seen that some PCPs do not change as the detection window moves. The PCB distribution of the wavelet reconstructed signal is more concentrated, and PCP statistics are shown in Fig. 7.

As shown at the top of Fig. 7, the PCP counts at the three abrupt are 281, 297, and 296, respectively, and are close to the size of the detection window, i.e., 300. Although the design displacement is small and at the same level as the standard deviation of the observation noise, all three design abrupt changes have been detected. As the displacement becomes larger, the statistical count increases, and the corresponding

where t denotes time. For RTK positioning mode, the horizontal positioning accuracy is 20–30 mm, whereas the vertical positioning accuracy is about 50 mm. Therefore, the standard deviation of observation noise in the simulation data is set to 50 mm.

1) Case 1—Significant Displacement: To evaluate the detection effect of this method on sudden displacements of different amplitudes, abrupt displacements of one time, two times, and three times the standard deviation are designed in the simulation data. At 500, 1000, and 1500 s, the displacements of 50, 100, and 150 mm are added, respectively. The simulation results are shown in Fig. 5.
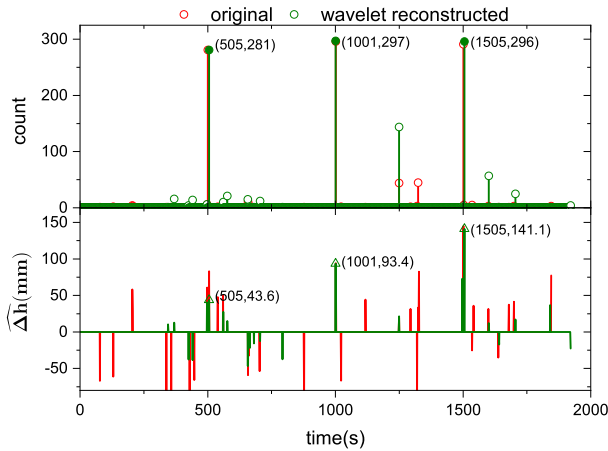
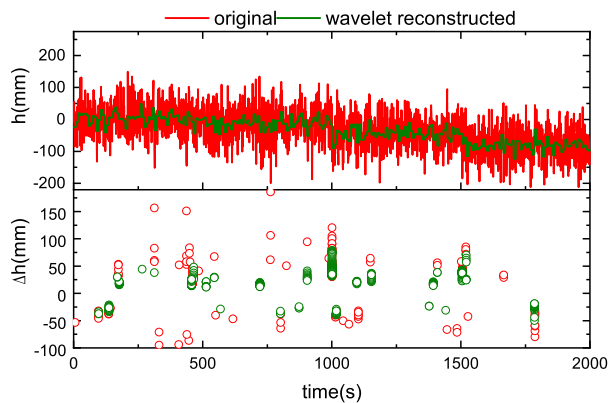Fig. 7. PCP statistics of simulation data with VT as the index.

Fig. 8. Detection result of small displacement simulation data with VT as the index.

uncertainty obtained according to (12) decreases. The three displacements obtained from the segmented window are 43.6, 93.4, and 141.1 mm, respectively. The error percentages of the three displacements extracted by the proposed method are 12.8%, 6.1%, and 5.9%, respectively. It can be seen from the above simulation experiment results that the proposed method can be effectively applied to displacement detection.

2) Case 2—Small Displacement: To further verify the performance of this method for small displacement, another set of data is simulated, and the displacements at 500, 1000, and 1500 s are set at 20, 30, and 40 mm, respectively. Other simulation options are consistent with those in the above simulation data. The simulation data are processed by the proposed method, and the results are shown in Figs. 8 and 9.

It can be seen from Fig. 8 that the displacement smaller than the standard deviation of the observation noise is difficult to be identified visually, even though reconstructed by wavelet transform. From the statistics of PCP, it can be seen that the statistical count is smaller than that of the previous one, and the identification of these small displacements is more easily affected by local disturbance. The statistical count of these small displacements is less than that of the previous experiment, and the corresponding uncertainty is greater than that of the previous experiment. The identified abrupt changes are at 457, 1001, and 1505 s. Lowering the threshold can identify these displacements, but the uncertainty is greater and
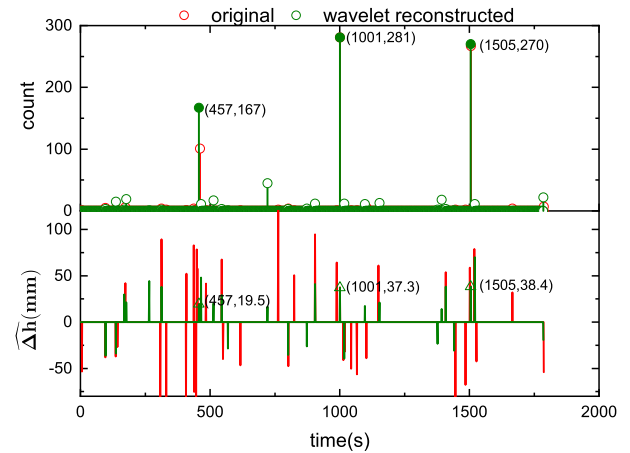

Fig. 9. PCP statistics of small displacement simulation data with VT as the index.

the false alarm rate is higher. The extracted displacements of the three abrupt changes at 457, 1001, and 1505 s are 19.5, 37.3, and 38.4 mm, respectively. The error percentages of the three displacements extracted by the proposed method are 2.5%, 9%, and 4%, respectively. From the above analysis, it can be seen that the displacement less than the standard deviation can be identified, but with greater uncertainty. The following section will give the results of the field experiment.

B. Field Experiments

1) Case 1—Ultrashort Baseline: The experiment was carried out on the roof of a building on the campus of Wuhan University. In the experiment, the equipment deployment is shown in Fig. 10. A hard plank is pressed with large stones to ensure that the plank remains as fixed as possible during moving the object hanging on the plank. One receiver antenna is fixed on the plank as a rover; the other receiver antenna is fixed on a tripod beside it as the base station. Both antennas are connected to BD992 original equipment manufacturer (OEM) boards on the table, and the OEM boards are connected to the laptops for data collection. As shown in subgraphs (c) and (d), the height of the antenna is measured with a tape before and after each movement of the object hanging on the plank. Besides, markers are made on the ground and on the antenna to ensure that the same position is referenced for each measurement. The sampling frequency of the GNSS receiver is set to 1 Hz. The whole experiment lasted for nearly 1 h, during which the object hanging on the plank was moved several times manually.

As shown in Fig. 10, the object hanging on the plank was moved toward the antenna in three steps. There is uncertainty in manual measurement. On the one hand, it comes from the reading error; on the other hand, because the displacement control device is not completely controllable, the antenna is always shacking under the influence of external environments, such as breeze and touching. Therefore, before and after moving the target, the antenna height from the ground was measured five times to reduce the uncertainty. The measured height and calculated displacement are shown in Table I. The GNSS observation data collected above are processed by the
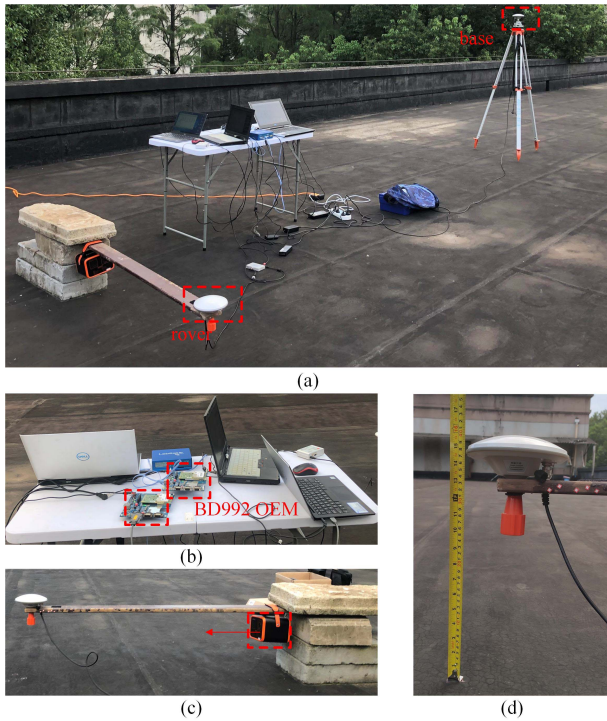
(a)

(b)

(c)

(d)

Fig. 10. Field experiment configuration. (a) Overview of the experiment. (b) BD992 OEM boards and data collection computers. (c) Displacement control device. (d) Displacement measurement.

TABLE I
MEASURED HEIGHT BEFORE AND AFTER EACH MOVEMENT OF THE OBJECT HANGING ON THE PLANK, UNIT (MM)

		1	2	3	4	5	mean
	h_0	368.5	368.9	369.0	368.9	369.0	368.9
Step 1	h_1	348.1	348.0	348.0	348.2	348.3	348.1
	Δh	20.4	20.9	21.0	20.7	20.7	20.7
	h_0	347.5	347.3	347.6	347.5	347.4	347.5
Step 2	h_1	326.1	326.3	326.1	326.0	326.1	326.1
	Δh	21.4	21.0	21.5	21.5	21.3	21.3
	h_0	325.0	325.1	324.9	325.0	325.2	325.0
Step 3	h_1	305.5	305.3	305.4	305.5	305.6	305.5
	Δh	19.5	19.8	19.5	19.5	19.6	19.6

open-source software RTKLIB [37], using relative real-time kinematic mode. The so-called processing unit is formed by the positioning result and is used as the input of wavelet reconstruction. The size of the detection window is set to 360. The wavelet reconstruction results as well as the obtained PCPs are shown in Fig. 11.

As shown at the top of Fig. 11, the measured data are much more complex than the simulated data. This is mainly caused by the complex spatiotemporal characteristics of GNSS measurement error, and there are unmodeled errors after data processing. Besides, breeze and touch during height measurement may cause the antenna's vibration. The results of wavelet reconstruction roughly show several abrupt changes of displacement. As shown at the bottom of Fig. 11, PCPs are mainly distributed at the abrupt change or local disturbance. PCPs obtained from time series reconstructed by the designed wavelet are less affected by local disturbance. PCP distribution
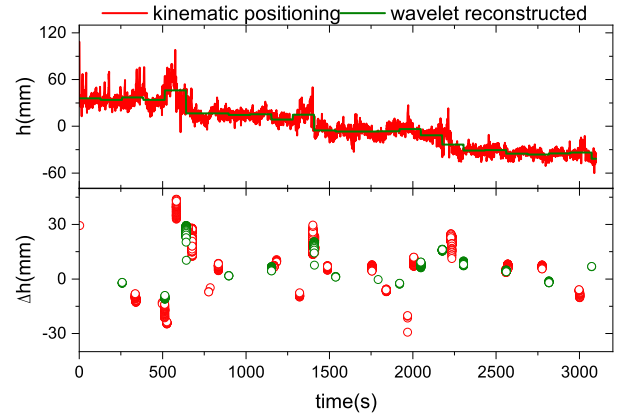

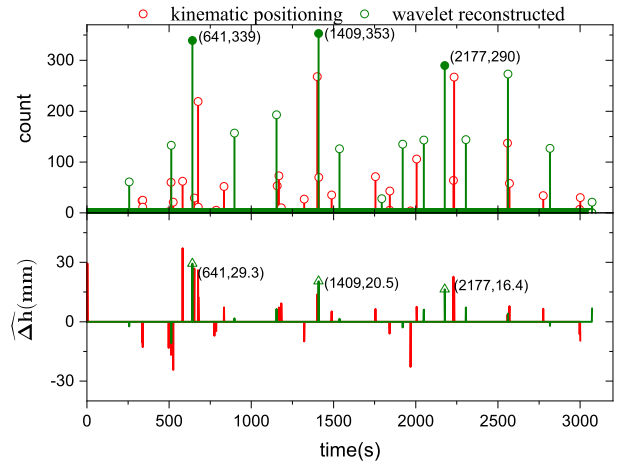Fig. 11. Detection result of field data with VT as the index.

Fig. 12. PCP statistics of field data with VT as the index.

of the wavelet reconstructed signal is more concentrated, and PCP statistics are shown in Fig. 12.

PCP count and displacement estimates are shown in Fig. 12. As shown at the top of Fig. 12, all manually triggered changes are detected, and the corresponding PCP counts are 339, 353, and 290, respectively. Besides, there are some local peaks, which may be caused by breeze and multipath during the experiment. The three displacements obtained from the segmented window are 29.3, 20.5, and 16.4 mm, respectively. As shown in Table I, the three displacements measured by tape are 20.7, 21.3, and 19.6 mm, respectively. The error percentages of the three displacements extracted by the proposed method are 41.5%, 3.76%, and 16.3%, respectively. The first displacement error is not at the same level as the other two extracted displacement errors, which may be caused by out of sync between the measured displacement time and segmented time.

2) Case 2—Short Baseline: To further explore the impact of baseline length on this method, we have used a continuous operating reference station (CORS) as the base station, which is about 6.3 km away from the rover station. The reference station is located on the campus of Hubei University, and the sampling rate of the receiver is also 1 Hz. To facilitate comparison, the data corresponding to the time range in the previous experiment are selected for processing. The data
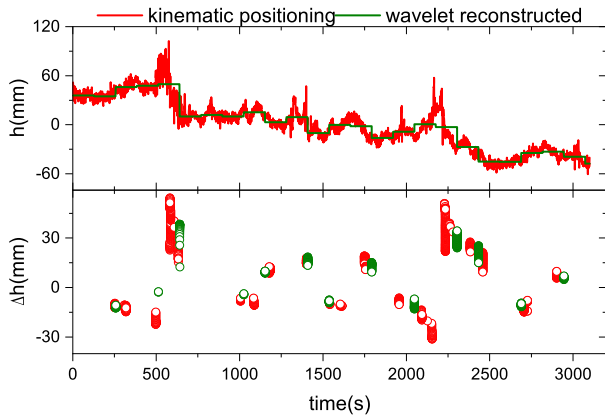
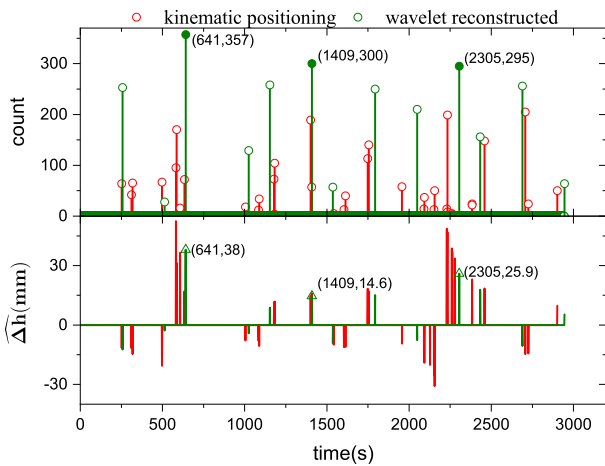Fig. 13. Detection result of a longer baseline with VT as the index.

Fig. 14. PCP statistics of a longer baseline with VT as the index.

processing is the same as above, except that the data of the base station are replaced by the data of the CORS station. The detection result, as well as the PCP statistics, are shown in Figs. 13 and 14, respectively.

Compared with the time series in Fig. 11, it can be seen from Fig. 13 that the noise level of the time series is higher than that of the ultrashort baseline. This is mainly due to the influence of atmospheric error that has not been eliminated. Similar to the ultrashort baseline, PCPs are mainly distributed at the abrupt and local disturbance. Compared with Fig. 12, the local disturbance at the top of Fig. 14 is more serious, but the abrupt can still be identified. The three extracted displacements are 38, 14.6, and 25.9 mm, respectively. The error percentages of the three displacements are 83.6%, 31.6%, and 32.1%, respectively. Similar to the ultrashort baseline, the first displacement error is not at the same level as the other two extracted displacement errors, which is mainly caused by out of sync between the measured displacement time and segmented time. As can be seen from the top of Fig. 13, the variance of the segmentation window in the first abrupt is larger than the other two.

It can be seen from the above results that the proposed method can accurately detect displacement changes. When the segmentation window is stable, the displacement obtained by the average of the segmentation window can reach
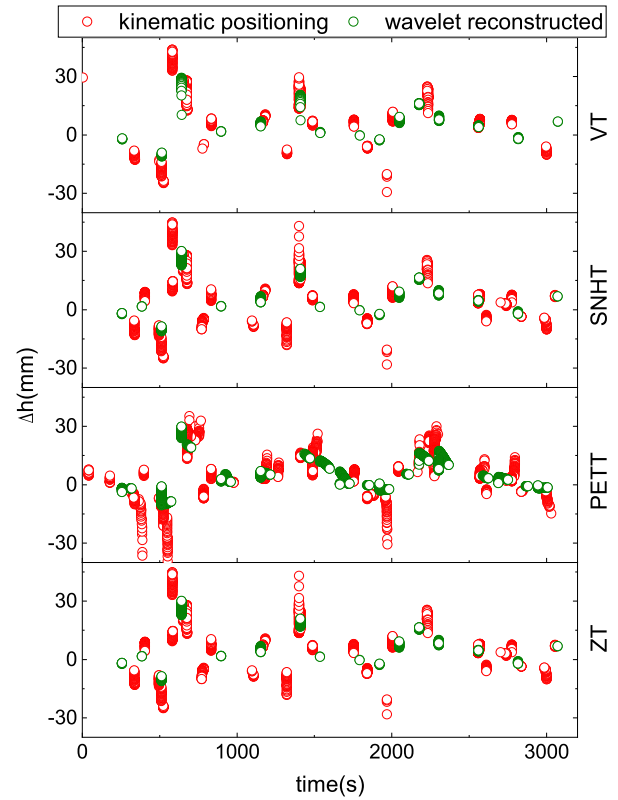

Fig. 15. PCPs for various segmentation indices.

subcentimeter accuracy. However, local disturbances in the detection window will cause a decrease in the accuracy of the extracted displacement. The influence of local disturbance can be suppressed by wavelet reconstruction. We will discuss the factors that influence detection results in the following section.

IV. DISCUSSION

In the data processing of the field experiments above, the segmentation index of the detection window is only set to VT, so the influence of various indices on the detection result will be discussed here. Besides, the effect of the detection window size on the detection results will also be discussed here.

A. Different Segmentation Indices

The proposed method is executed based on the ultrashort baseline data when the window segmentation index is set to VT, SNHT, PETT, and ZT. The detection window size remains unchanged and is always set to 360. PCPs, as well as the PCP count, are shown in Figs. 15 and 16, respectively.

As shown in Figs. 15 and 16, the performance of the PETT is weaker than the other three indices. The PETT index is susceptible to interference from local disturbances, and the corresponding PCPs are more scattered than other indices. The PCP count of the PETT index at the abrupt change is also significantly smaller than other indices. VT, SNHT, and ZT have s similar performance, but VT is less affected by local small disturbance than the other two indices. Therefore, it is recommended to use VT as the index of window segmentation in the proposed method.
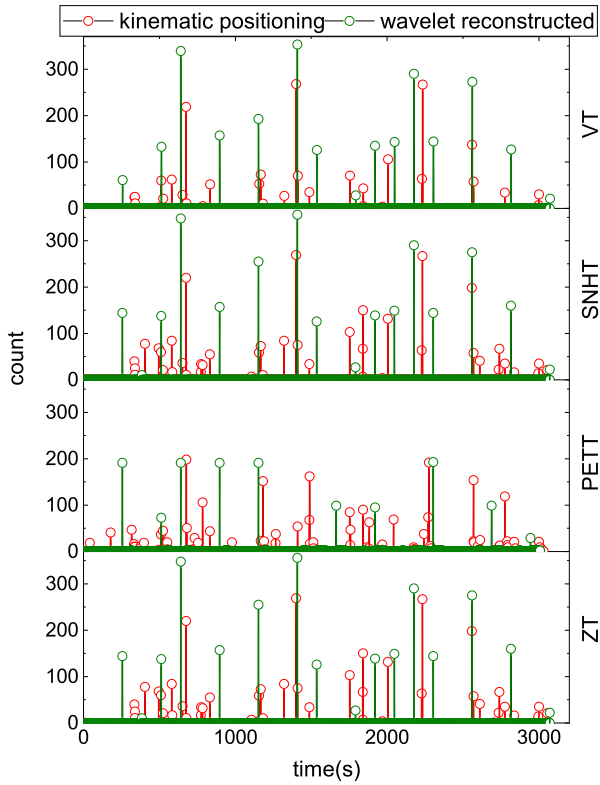
Fig. 16. PCP count for various segmentation indices.

Fig. 17. PCPs of small displacement simulation data with VT as the index for various detection window sizes.

B. Set the Appropriate Detection Window Size

To further investigate the relationship between the detection window size and the captured PCPs, we set the size of the detection window between 50 and 750 and then get the PCPs from the proposed method. The small displacement simulation data and the ultrashort baseline field data are processed separately. For the convenience of comparison, the normalized PCP count is given, which can be obtained by the ratio of absolute PCB count to window size. The statistical results of the small displacement simulation data are shown in Figs. 17 and 18.

It can be seen from Fig. 17 that when the size of the detection window is small, many local disturbances appear due to the influence of observation noise. With the increase of the detection window size, the PCPs gradually tend to be stable, and the local disturbance decreases gradually. Compared with the original time series, the PCP distribution obtained from the wavelet reconstruction time series is more concentrated. It can be seen from Fig. 18 that with the increase of the detection window size, the PCPs count caused by local disturbance is decreasing. Since the designed wavelet filters out the high-frequency noise, the normalized PCP count of the wavelet reconstruction signal is larger. When the window size is small, each small-displacement step in the wavelet reconstruction time series is reflected in the normalized PCP count. With the increase of detection window size, the influence of these small-displacement steps gradually weakens. The statistical results of the ultrashort baseline field data are shown in Figs. 19 and 20.
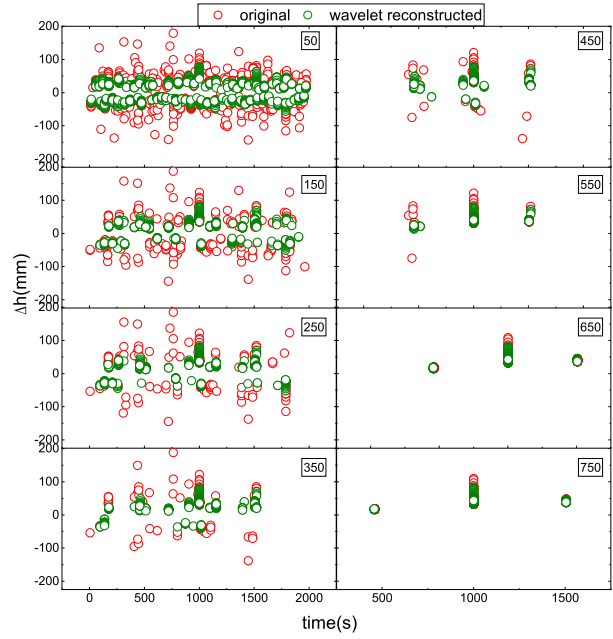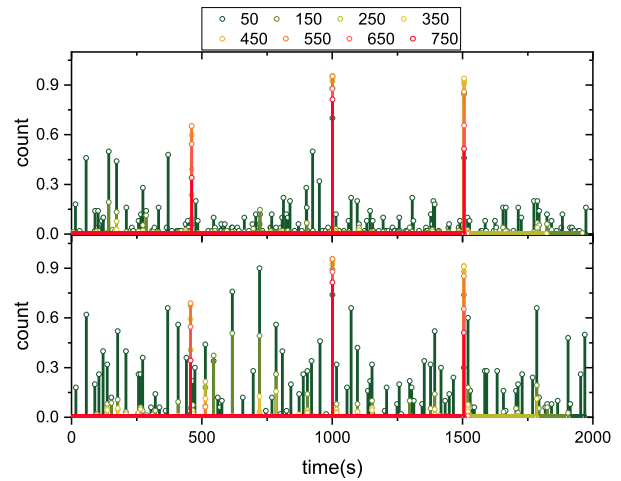

Fig. 18. Normalized count of PCPs of small displacement simulation data with VT as the index for various detection window size. Top: original. Bottom: wavelet reconstructed.

Similarly, it can be seen from Figs. 19 and 20 that increasing the window size helps to weaken the local disturbance. However, large windows can cause some problems. On the one hand, a large window size will reduce the detection granularity because multiple displacements may be located in the same detection window. On the other hand, a large window size will reduce the timeliness of detection.

From the above discussion, it can be concluded that displacement detection is affected by the detection window size. When the window size is small, the change detection is significantly affected by the observation noise. A large window size helps to weaken the local disturbance. However, the window size directly affects the timeliness of displacement detection, and the larger the window size, the worse the timeliness. Besides, a large window size will reduce the detection granularity. Therefore, it is recommended to set
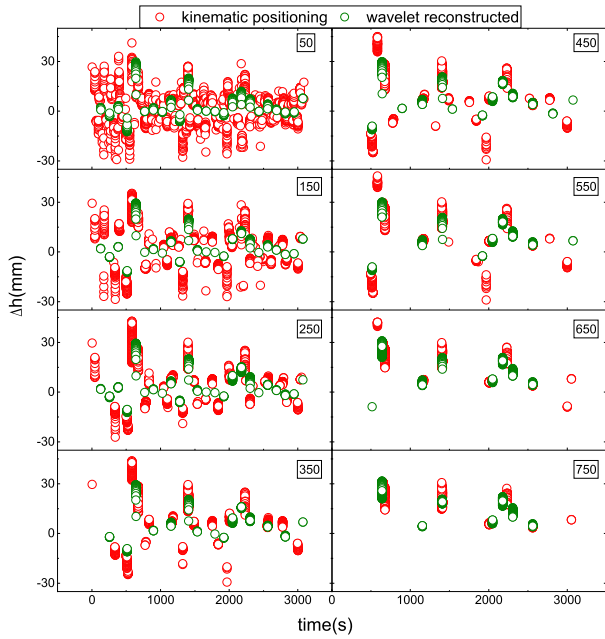
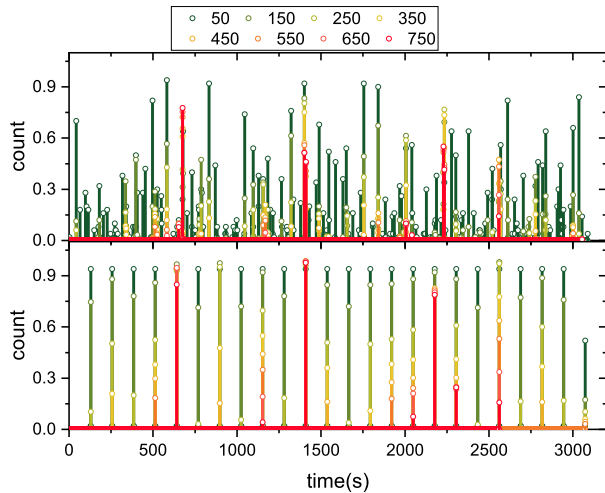Fig. 19. PCPs of ultrashort baseline field data with VT as the index for various detection window sizes.

Fig. 20. Normalized count of PCPs of ultrashort baseline field data with VT as the index for various detection window sizes. Top: kinematic positioning. Bottom: wavelet reconstructed.

the window size according to the detection granularity and the allowed time delay. To summarize, this study and the proposed methodology differ from previous research efforts in several aspects.

1) Displacement identification and extraction are implemented through the segmentation of the GNSS kinematic positioning time series. Compared with the traditional model, this reduces the influence of the gross error and observation noise.

2) Displacement identification is based on the statistics of PCP obtained by time series segmentation, so as to reduce the influence of local disturbance.

3) Displacement extraction is based on the mean value of segments, and its accuracy is better than that of single-epoch displacement extraction.

4) The size of the segmentation window can be flexibly set according to the requirements of detection granularity and timeliness.

One limitation of this method is the detection of small displacement. For the detection of small displacement, wavelet cannot effectively reconstruct the abrupt component. The influence of local disturbance can be reduced by increasing the size of the detection window, but it will increase the delay time and reduce the detection granularity. Besides, with the increase of window size, the trend term in GNSS time series cannot be ignored. Further work needs to be done to eliminate the influence of these low-frequency trend terms, and longer experiments needed to be carried out to verify the small-displacement detection in the follow-up work. In addition, the current method of displacement detection and displacement extraction is separate and complex. In the follow-up work, Bayesian inference will be considered to simplify the process of displacement detection and displacement extraction.

V. CONCLUSION

In this article, we developed a method aiming at short-term landslide monitoring based on GNSS kinematic positioning and time series segmentation. The detection window is formed by the current epoch and the previous epochs coordinates obtained by GNSS kinematic positioning. The segmentation point is obtained by segmentation of the detection window, and a test is conducted to determine whether the segmentation point is a change point. To verify the approach, we conducted two sets of experiments. In the simulation experiment, the observation data that are affected by both noise and a trend item were constructed. The results show that the three abrupt changes designed can be accurately detected. In the field experiment, RTK kinematic positioning mode was used to process observations, and two baselines with different lengths were processed. The results show that the method can accurately detect the manually trigger displacement, and the accuracy of the extracted displacement can reach the subcentimeter level. Finally, we discussed the main issues of the proposed method: window segmentation indices and detection window size. VT is less affected by local small disturbance than the other indices, and it is recommended to use VT as the index of window segmentation in the proposed method. When the detection window size is small, the change detection is significantly affected by local disturbance. Wavelet reconstruction and increasing window size are recommended to suppress the influence of local disturbance. For small displacement, wavelets can not effectively reconstruct the abrupt component but it is also suggested to increase the window size to detect the original time series.

REFERENCES

[1] J. F. Shroder, *Landslide Hazards, Risks, and Disasters*. New York, NY, USA: Academic, 2014.

[2] J. J. Clague and D. Stead, *Landslides: Types, Mechanisms and Modeling*. Cambridge, U.K.: Cambridge Univ. Press, 2012.

[3] Y. Sugimoto *et al.*, "Development of GPS positioning system 'PRESTAR,'" *IEEE Trans. Instrum. Meas.*, vol. 38, no. 2, pp. 644–647, Apr. 1989.

[4] N. Shen *et al.*, "A review of global navigation satellite system (GNSS)-based dynamic monitoring technologies for structural health monitoring," *Remote Sens.*, vol. 11, no. 9, p. 1001, Apr. 2019.

[5] P. Giri, K. Ng, and W. Phillips, "Wireless sensor network system for landslide monitoring and warning," *IEEE Trans. Instrum. Meas.*, vol. 68, no. 4, pp. 1210–1220, Apr. 2019.

[6] J. A. Gili, J. Corominas, and J. Rius, "Using global positioning system techniques in landslide monitoring," *Eng. Geol.*, vol. 55, no. 3, pp. 167–192, Feb. 2000.

[7] H. Z. Abidin, H. Andreas, M. Gamal, S. Surono, and M. Hendrasto, "Studying landslide displacements in Megamendung (Indonesia) using GPS survey method," *J. Eng. Technol. Sci.*, vol. 36, no. 2, pp. 109–123, 2004.

[8] M.-B. Su, I.-H. Chen, and C.-H. Liao, "Using TDR cables and GPS for landslide monitoring in high mountain area," *J. Geotech. Geoenvironmental Eng.*, vol. 135, no. 8, pp. 1113–1121, Aug. 2009.

[9] M. S. Rawat, V. Joshi, B. S. Rawat, and K. Kumar, "Landslide movement monitoring using GPS technology: A case study of Bakthang landslide, Gangtok, East Sikkim, India," *J. Develop. Agricult. Econ.*, vol. 3, no. 5, pp. 194–200, 2011.

[10] G. Wang, "GPS landslide monitoring: Single base vs. network solutions—A case study based on the Puerto Rico and Virgin Islands permanent GPS network," *J. Geodetic Sci.*, vol. 1, no. 3, pp. 191–203, Jan. 2011.

[11] H.-C. Lee, K.-H. Ke, Y.-M. Fang, B.-J. Lee, and T.-C. Chan, "Open-source wireless sensor system for long-term monitoring of slope movement," *IEEE Trans. Instrum. Meas.*, vol. 66, no. 4, pp. 767–776, Apr. 2017.

[12] M. Lytvyn, C. Pollabauer, M. Troger, K. Landfahrer, L. Hormann, and C. Steger, "Real-time landslide monitoring using single-frequency PPP: Proof of concept," in *Proc. 6th ESA Workshop Satell. Navigat. Technol. (Navitec) Eur. Workshop GNSS Signals Signal Process.*, Dec. 2012, pp. 1–6.

[13] R. Xiao and X. He, "Real-time landslide monitoring of Pubugou hydropower resettlement zone using continuous GPS," *Natural Hazards*, vol. 69, no. 3, pp. 1647–1660, Dec. 2013.

[14] L. Li and H. Kuhlmann, "Deformation detection in the GPS real-time series by the multiple Kalman filters model," *J. Surveying Eng.*, vol. 136, no. 4, pp. 157–164, Nov. 2010.

[15] A. Cina and M. Piras, "Performance of low-cost GNSS receiver for landslides monitoring: Test and results," *Geomatics, Natural Hazards Risk*, vol. 6, nos. 5–7, pp. 497–514, Jul. 2015.

[16] T. Bellone, P. Dabove, A. M. Manzino, and C. Taglioretti, "Real-time monitoring for fast deformations using GNSS low-cost receivers," *Geomatics, Natural Hazards Risk*, vol. 7, no. 2, pp. 458–470, Mar. 2016.

[17] P. Dabove and A. M. Manzino, "Fast displacements detection techniques considering mass-market GPS L1 receivers," in *Proc. Int. Conf. Geogr. Inf. Syst. Theory, Appl. Manage.*, vol. 741, 2016, pp. 1–14.

[18] P. J. Teunissen and O. Montenbruck, *Springer Handbook of Global Navigation Satellite Systems*. Cham, Switzerland: Springer, 2017.

[19] Q. Xu, M. Tang, K. Xu, and X. Huang, "Research on space-time evolution laws and early warning-prediction of landslides," *Chin. J. Rock Mech. Eng.*, vol. 27, no. 6, pp. 1104–1112, 2008.

[20] Y. Li, R. Sun, K. Yin, Y. Xu, B. Chai, and L. Xiao, "Forecasting of landslide displacements using a chaos theory based wavelet analysis-Volterra filter model," *Sci. Rep.*, vol. 9, no. 1, p. 19853, Dec. 2019.

[21] D. M. Cruden and D. J. Varnes, "Landslide types and processes," in *Landslides: Investigation and Mitigation*, no. 247. Washington, DC, USA, 1996, ch. 3.

[22] W. Li, "A study on key technology of high precision GPS monitoring for geological hazard," *Acta Geodaetica et Cartographica Sinica*, vol. 44, no. 7, p. 826, 2015.

[23] S. Zhang et al., "Real-time safety evaluation for slope during construction using numerical forecast and sensor monitoring platform," *Sensors*, vol. 18, no. 9, p. 2978, Sep. 2018.

[24] R. Killick, P. Fearnhead, and I. A. Eckley, "Optimal detection of changepoints with a linear computational cost," *J. Amer. Stat. Assoc.*, vol. 107, no. 500, pp. 1590–1598, Dec. 2012.

[25] M. Lavielle, "Using penalized contrasts for the change-point problem," *Signal Process.*, vol. 85, no. 8, pp. 1501–1510, Aug. 2005.

[26] M. N. Khaliq and T. B. M. J. Ouarda, "On the critical values of the standard normal homogeneity test (SNHT)," *Int. J. Climatol.*, vol. 27, no. 5, pp. 681–687, 2007.

[27] I. Mallkpour and G. Villarini, "A simulation study to examine the sensitivity of the Pettitt test to detect abrupt changes in mean," *Hydrolog. Sci. J.*, vol. 61, no. 2, pp. 245–254, Jan. 2016.

[28] B. Hofmann-Wellenhof, H. Lichtenegger, and E. Wasle, *GNSS—Global Navigation Satellite Systems: GPS, GLONASS, Galileo, and More.* New York, NY, USA: Springer, 2007.

[29] P. J. G. Teunissen, "The least-squares ambiguity decorrelation adjustment: A method for fast GPS integer ambiguity estimation," *J. Geodesy*, vol. 70, nos. 1–2, pp. 65–82, Nov. 1995.

[30] L. Wang, S. Verhagen, and Y. Feng, "Ambiguity acceptance testing: A comparison of the ratio test and difference test," in *China Satellite Navigation Conference (CSNC) 2014 Proceedings: Volume II* (Lecture Notes in Electrical Engineering), vol. 304. Berlin, Germany: Springer, 2014, pp. 313–330.

[31] L. Wang et al., "Improving GNSS ambiguity acceptance test performance with the generalized difference test approach," *Sensors*, vol. 18, no. 9, p. 3018, Sep. 2018.

[32] M. S. Grewal and A. P. Andrews, *Kalman Filtering: Theory and Practice With MATLAB*. Hoboken, NJ, USA: Wiley, 2014.

[33] N. Shen et al., "Site-specific real-time GPS multipath mitigation based on coordinate time series window matching," *GPS Solutions*, vol. 24, no. 3, pp. 1–14, Jul. 2020.

[34] P. S. Addison, *The Illustrated Wavelet Transform Handbook: Introductory Theory and Applications in Science, Engineering, Medicine and Finance*, 2nd ed. Boca Raton, FL, USA: CRC Press, 2016.

[35] M. Stephane, *A Wavelet Tour of Signal Processing: The Sparse Way*. Burlington: Elsevier, 1999.

[36] X. Z and Y. Y, "Wavelet basis selection method for fault signal detection," *Control Eng. China*, vol. 10, no. 4, pp. 308–311, 2003.

[37] T. Takasu. (2013). *RTKLIB: An Open Source Program Package for GNSS Positioning*. [Online]. Available: http://www.rtklib.com/

Nan Shen is currently pursuing the Ph.D. degree with the State Key Laboratory of Information Engineering in Surveying, Mapping and Remote Sensing, Wuhan University, Wuhan, China.

His research interests include GNSS high-precision navigation and positioning technology, real-time mitigation of site-specific errors, intelligent mitigation of GNSS unmodeled errors, interactive multimodel vibration detection, and extraction technology; software-defined receiver design; and integrated navigation and positioning technology of GNSS, INS, and vision.

Liang Chen was a Senior Research Scientist with the Department of Navigation and Positioning, Finnish Geodetic Institute, Kirkkonummi, Finland. He is currently a Professor with the State Key Laboratory of Information Engineering in Surveying, Mapping, and Remote Sensing, Wuhan University, Wuhan, China. He has published over 70 scientific articles and 5 book chapters. His current research interests include indoor positioning, wireless positioning, sensor fusion, and location-based services.

Prof. Chen is currently an Associate Editor of *Journal of Navigation* and *Navigation-Journal of Institute of Navigation*.

Lei Wang (Member, IEEE) received the Ph.D. degree from the Queensland University of Technology, Brisbane, QLD, Australia, in 2015.

He is currently an Associate Research Fellow with Wuhan University, Wuhan, China. He is the major Designer of navigation augmentation system on the Luojia-1A Satellite. His research interests include GNSS precise positioning, LEO navigation augmentation, LEO precise orbit determination, and indoor positioning systems. He has published more than 50 scientific research articles and applied 13 patents.

Dr. Wang serves as a reviewer for many journals, including IEEE ACCESS, IEEE TRANSACTIONS ON AEROSPACE AND ELECTRONIC SYSTEMS, *Journal of Intelligent Transportation Systems*, *Measurements*, *Measurement Science and Technology*, *Sensors*, *Chinese Journal of Aeronautics*, *Journal of Navigation*, and *Geo-Spatial Information Science*.

Hao Hu is currently pursuing the master's degree with the State Key Laboratory of Information Engineering in Surveying, Mapping and Remote Sensing, Wuhan University, Wuhan, China.

His main research direction includes software-defined receivers.

Xiangchen Lu is currently pursuing the master's degree with the State Key Laboratory of Information Engineering in Surveying, Mapping and Remote Sensing, Wuhan University, Wuhan, China.

His main research direction includes software-defined receivers.

Chuang Qian received the Ph.D. degree from Wuhan University.

He is currently a Researcher with the Intelligent Transport Systems Research Center, Wuhan University of Technology. His research interests focus on GNSS high-precision navigation and positioning technology, GNSS atmospheric error modeling, GNSS time series analysis, GNSS engineering application, and multi-source navigation.

Jingbin Liu was a Senior Research Scientist with the Department of Navigation and Positioning, Finnish Geodetic Institute, Kirkkonummi, Finland. He is currently a Professor with the State Key Laboratory of Information Engineering in Surveying, Mapping, and Remote Sensing, Wuhan University, Wuhan, China. He has published over 60 scientific articles and 4 book chapters. His current research interests include ubiquitous positioning, mobile mapping, smartphone navigation, spatial perception, indoor positioning, simultaneous localization and mapping, and GNSS positioning.
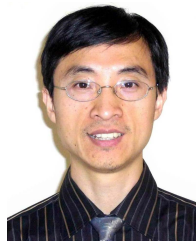
Shuanggen Jin (Member, IEEE) was born in Anhui, China, in September 1974. He received the B.Sc. degree in geodesy from Wuhan University, Wuhan, China, in 1999, and the Ph.D. degree in geodesy from the University of Chinese Academy of Sciences, Beijing, China, in 2003.

He is currently a Professor with the Shanghai Astronomical Observatory, Chinese Academy of Sciences (CAS), Shanghai, China, a member of Academia Europaea, a member of the European Academy of Science, and a member of the Russian Academy of Natural Sciences. He has more than 400 articles in international peer-reviewed journals and proceedings, holds 10 patents/software copyrights, and 10 books/monographs with more than 6000 citations. His main research interests include satellite navigation, remote sensing, and space/planetary exploration.

Dr. Jin was a Fellow of the International Association of Geodesy (IAG) in 2011 and the International Union of Geodesy and Geophysics (IUGG) in 2019. He has been the President of the International Association of Planetary Sciences (IAPS) (2015–2019), the President of the International Association of CPGPS (2016–2017), the Chair of the IUGG Union Commission on Planetary Sciences (UCPS) (2015–2019), and the Vice-President of the International Association of Geodesy (IAG) Commission 2 (2015–2019). He has received the Special Prize of Korea Astronomy and Space Science Institute in 2006, the Hundred-Talent Program of Chinese Academy of Sciences in 2010, the Jiangsu Distinguished Professor in 2018, the First Prize of Satellite Navigation and Positioning Progress Award in 2017, and the First Prize of China Overseas Chinese Contribution Award in 2018. He has been the Editor-in-Chief of the *International Journal of Geosciences* since 2010, and the Journal of Environmental and Earth Sciences since 2018, an Associate Editor of the IEEE TRANSACTIONS ON GEOSCIENCE AND REMOTE SENSING since 2014, *The Journal of Navigation* since 2014, and *Advances in Space Research* (2013–2017), and an Editorial Board Member of *Remote Sensing* since 2017, *GPS Solutions* since 2016, the *Journal of Geodynamics* since 2014, and *Planetary and Space Science* since 2014.

Ruizhi Chen is currently a Professor and the Director of the State Key Laboratory of Information Engineering in Surveying, Mapping, and Remote Sensing, Wuhan University, Wuhan, China. Prior to that, he was an Endowed Chair Professor with Texas A&M University–Corpus Christi, USA, the Head and a Professor with the Department of Navigation and Positioning, Finnish Geodetic Institute, Kirkkonummi, Finland, and the Engineering Manager at Nokia, Espoo, Finland. He has published 2 books and more than 200 scientific articles. His current research interests include indoor positioning, satellite navigation, and location-based services.